

Identification of Attack-Specific Signatures in Adversarial Examples

Hossein Souri^{*1}, Pirazh Khorramshahi^{*1}, Chun Pong Lau¹, Micah Goldblum², Rama Chellappa¹

¹Johns Hopkins University, ²University of Maryland, College Park

{hsouril, pkhorr1, clau13, rchella4}@jhu.edu, goldblum@umd.edu

Abstract

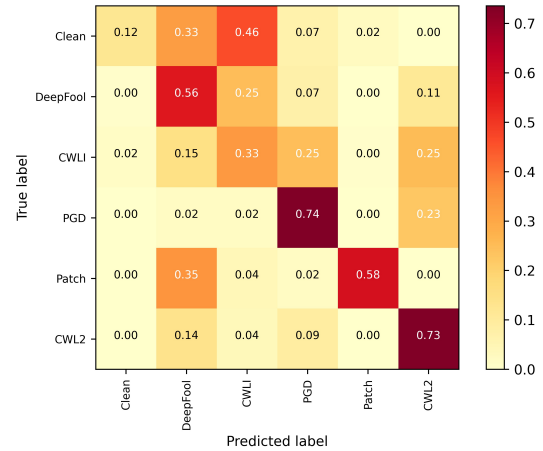
The adversarial attack literature contains a myriad of algorithms for crafting perturbations which yield pathological behavior in neural networks. In many cases, multiple algorithms target the same tasks and even enforce the same constraints. In this work, we show that different attack algorithms produce adversarial examples which are distinct not only in their effectiveness but also in how they qualitatively affect their victims. We begin by demonstrating that one can determine the attack algorithm that crafted an adversarial example. Then, we leverage recent advances in parameter-space saliency maps to show, both visually and quantitatively, that adversarial attack algorithms differ in which parts of the network and image they target. Our findings suggest that prospective adversarial attacks should be compared not only via their success rates at fooling models but also via deeper downstream effects they have on victims.

1. Introduction

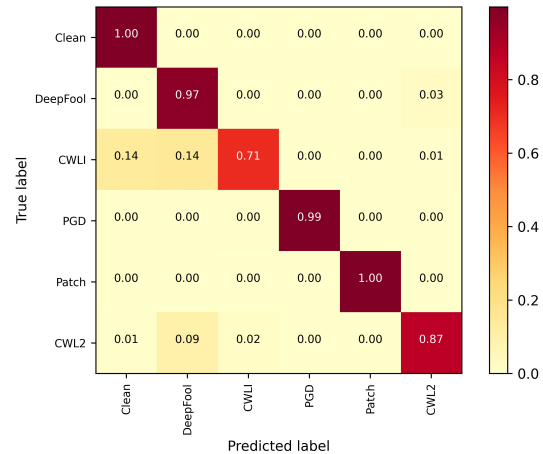
In recent years, neural networks and in particular Deep Convolutional Neural Networks (DCNN) have revolutionized the field of computer vision by outperforming almost all of the traditionally designed methods by a large margin across a variety of tasks including Image Recognition [18, 12], Object Detection [8, 22, 31], Object Tracking [40], Image Captioning [39], Face Recognition [30], Human Pose Estimation [27] and Action Recognition [34]. Despite their performance superiority, DCNNs are easily fooled by maliciously crafted adversarial examples [38].

To compromise DCNNs, a number of attacks have been proposed which generate adversarial images that are visually indistinguishable from clean images. Among these attacks are Projected Gradient Descent (PGD) [23], DeepFool (DF) [25], Carlini & Wagner (CW) [2], and Adversarial Patch [1, 14]. The emergence of adversarial attacks has motivated the development of numerous defense methods for protecting DCNNs against adversaries. Countermeasures

^{*}The first two authors have contributed equally to this work.



(a)



(b)

Figure 1. (a) Confusion matrix of a ResNet18 network trained on adversarial images for the task of attack type classification. Accuracy of this network is 57.55%. (b) Confusion matrix of another ResNet18 network trained on the concatenation of adversarial images with their respective perturbations for the similar task of attack type classification. This network yields the accuracy of 94.23%.

against adversaries can be categorized into *Robust Optimization*[21], *Gradient Masking*[29], *Adversarial Training* [23], and *Adversarial Example Detection* [42]. Apart from

designing attacks and their respective defense methods, we are interested in understanding how different attacks impact their victims in distinct ways and whether we can distinguish the type of an attack based on its resulting adversarial examples. The most straightforward signature of an attack resides in the perturbation it creates on top of the clean sample. However, due to imperceptibility constraints, perturbations are typically much smaller than the original signal. Therefore, it is challenging to recognize and isolate the exact perturbation from the adversarial example alone.

To investigate whether adversarial attack algorithms can be distinguished via their perturbations and to further understand how unique the signatures in the resulting adversarial examples are, we conduct the following two experiments. We create five adversarial versions of the CIFAR-10 dataset [17] using popular adversarial attacks along with multiple classification models for generating perturbations, multiple attack constraints, and multiple attack hyper-parameters. Then, in the first experiment, we train a classifier to classify images into their respective attack types or the clean class in case they are sampled from the clean training data. In the second experiment, we instead input the concatenation of an adversarial image with its respective perturbation. Figures 1a and 1b show the confusion matrices of attack classifiers from each of these two experiments. From Figure 1a, we observe that the network trained only on the adversarial examples struggles to classify the adversarial images correctly, and in particular, the network fails to distinguish clean samples. On the contrary, Figure 1b demonstrates the high performance of the classifier over the concatenation of perturbations with their respective adversarial examples. As the network in the second experiment, can recognize attacks much more effectively, *i.e.* 94.23% compared to 57.55% recognition accuracy, we conclude that the signature of each attack is unique and encoded in its perturbations.

We note that adversarial perturbations, used in this second experiment, are not readily available for practitioners due to the fact that once an attack occurs, only the corresponding adversarial image is accessible. Therefore, we develop a pipeline for isolating the perturbation from adversarial images based on image residual learning, which has been shown to be an effective tool in capturing small-scale yet important details [15]. Residual images enable us to identify attack algorithms from the adversarial example alone effectively.

The observation that adversarial attack algorithms generate distinct examples motivates us to explore how these attacks manifest their differences in the downstream behavior of victim models. Specifically, we adopt the parameter-space saliency maps method [20] to understand which parts of the victim model are targeted by a particular attack model. We find that attack algorithms exhibit not only superficially distinguishable image patterns but also influence

their victims in unique qualitative fashions.

The rest of the paper is organized as follows. In Section 2, we review recent related works in the area of adversarial attacks, defenses and saliency maps. Next, we discuss the datasets and adversarial attack algorithms which are used in this work in section 3. Section 4 describes our proposed method for the estimation of adversarial perturbations. Throughout section 5, we investigate how different attack methods manipulate the behaviour of neural networks. Finally we conclude the paper in section 6.

2. Related Work

2.1. Adversarial Attacks

Adversarial attacks perturb inputs to models in order to degrade their performance [38]. Typical attacks employ optimizers to maximize the model’s loss or a surrogate loss with respect to the input constrained to a set which ensures that the resulting adversarial example is hard to be distinguished from its original counterpart. One famous attack, projected gradient descent (PGD), involves an alternating procedure of signed gradient ascent steps on cross-entropy loss and projection onto the constraint set, typically an ℓ_∞ ball surrounding the base image [23]. [2] explores numerous alternative surrogate objective functions and finds that surrogates can improve the effectiveness of adversaries over directly optimizing cross-entropy loss. Adversarial attacks have been proposed both to probe the robustness of neural networks [43, 28] and to compromise their security [10, 4].

In response to this looming threat, a number of defenses have been proposed [23, 44, 9]. Another line of defensive works involves detecting adversarial examples to alert critical systems [24, 7, 11]. While this direction may appear similar to our own on the surface, our methods do not focus on distinguishing adversarial and clean examples but instead seek to distinguish adversarial examples generated via different algorithms from each other. Moreover, our methods are not intended as defensive tools but instead provide exploratory observations regarding the nature of adversarial examples.

2.2. Saliency Maps

A major component of our analysis relies on *saliency maps*. Typical saliency maps identify the extent to which each input feature (*e.g.* pixel) of a particular sample influences a model’s output [33, 32]. One recent work instead identifies the extent to which each model parameter is responsible for model misbehaviors [20]. This tool allows us to examine precisely which components in a neural network are affected by an adversarial example and also how these components interact with the input. We find that, in fact, different adversarial attacks influence different parts of the network, even when we average over thousands of samples.

3. Experimental Setup

3.1. Datasets

In this study, we consider the CIFAR-10 and Tiny ImageNet [41] datasets. Tiny ImageNet is a smaller subset of the ImageNet benchmark [5] with 200 classes. Compared to CIFAR-10, Tiny ImageNet has a higher diversity and larger dimensionality, *i.e.* images are of the size 64×64 .

3.2. Adversarial Attacks

To generate adversarial perturbations required for training and testing in our experiments, we considered the following attacks:

- **PGD**[23] produces adversarial perturbation, *i.e.* δ , in an iterative fashion in multiple steps. At each iteration, a step is taken in the signed gradient direction to maximize the cross-entropy loss of the victim model. After every such step, the attacker projects δ onto the ℓ_∞ ball in order to ensure that the generated adversarial sample I_{adv} remains within the constraint space surrounding clean image I_c .
- **DeepFool**[25] attempts to iteratively find a route for I_c to pass the decision boundary drawn by the an image classification model. Here, δ can be computed as the summation of perturbations (normal vector of the linearized decision boundary) found at each iteration.
- **CW** [2] is a computationally expensive iterative approach to generating adversarial samples which instead opts for a surrogate objective formed by subtracting the highest incorrect logit from the logit corresponding to the correct class. In this work, we consider L_2 and L_∞ norm versions of the CW attack.
- **Adversarial Patch**[14] selects a random location within a clean sample to be overlaid with a patch with desired height and width. In addition, we ensure that the crafted patch remains within the ℓ_∞ -ball surrounding the corresponding clean image in the patch location.

4. Adversarial Perturbation Estimation

Adversarial perturbations are relatively sparse and generally carry much lower energy compared to the original image’s content as seen in Figure 2. In addition, Figure 1 demonstrates the advantage of including perturbations over adversarial images alone when classifying attack algorithms. However, in reality, networks do not have access to the adversarial perturbations. Therefore, we propose a method for estimating adversarial perturbations in which the roles of signal and noise are switched. In other words, rather than treating clean images as the signal of interest

and adversarial perturbation as noise, we switch our focus to first recovering perturbations and then using them to classify attack algorithms.

In an effort to estimate adversarial perturbations, recognize the presence of attacks, and determine their parent algorithms, we develop Reverse Engineering of Deceptions via Residual Learning (REDRL) where a set of constraints are introduced to help the Reconstruction network G in recovering the clean image components from adversarial images so that adversarial perturbations can be isolated. The pipeline of REDRL is outlined in Figure 3 which consists of four main components, namely *image reconstruction*, *image classification*, *feature reconstruction*, and *residual recognition*. During training, REDRL takes an image as the input $I_{adv} = I_c + \delta$ where I_c and δ denote a clean image and adversarial perturbation, respectively. REDRL tries to salvage the content in the input image I_{adv} so that the generated image I_g lies close to the manifold of clean images. To ensure this property, REDRL constrains the generated image with several objectives, which we now enumerate.

4.1. Image Reconstruction

First, I_g should lie close to I_c in pixel space. Different distance metrics can be used for this purpose; however, we choose the L_1 distance similar to the work of Pix2Pix [13]. For the architecture of reconstructor G , we leverage prior work in super-resolution [19]. Therefore, G is composed of a set of identical residual blocks without batch normalization that are preceded and followed by two convolutional layers with Leaky ReLU non-linearities. Note that there is no skip connection in G as we would like to eliminate any direct transportation of adversarial perturbations. In addition, the spatial size of the input image is maintained during the reconstruction process. Our image reconstruction objective encourages G to recover $I_g = G(I_{adv})$ by minimizing the following function:

$$\mathcal{L}_R(G) = \mathbb{E}_{I_c, \delta} \left[\|I_c - G(I_c + \delta)\|_1 \right] \quad (1)$$

4.2. Feature Reconstruction

In addition to the previous pixel-space objective, I_g should lie close to I_c in the feature space of a neural network feature extractor so that I_g is semantically similar to I_c . Inspired by the work of [26], we employ the feature space of the third convolutional block of an ImageNet-trained VGG16 network [35] \mathcal{F} and L_2 distance to minimize the feature distortion between I_g and I_c . Subsequently, our feature reconstruction objective encourages G to minimize the following loss function:

$$\mathcal{L}_F(G) = \mathbb{E}_{I_c, \delta} \left[\|\mathcal{F}(I_c) - \mathcal{F}(G(I_c + \delta))\|_2 \right] \quad (2)$$

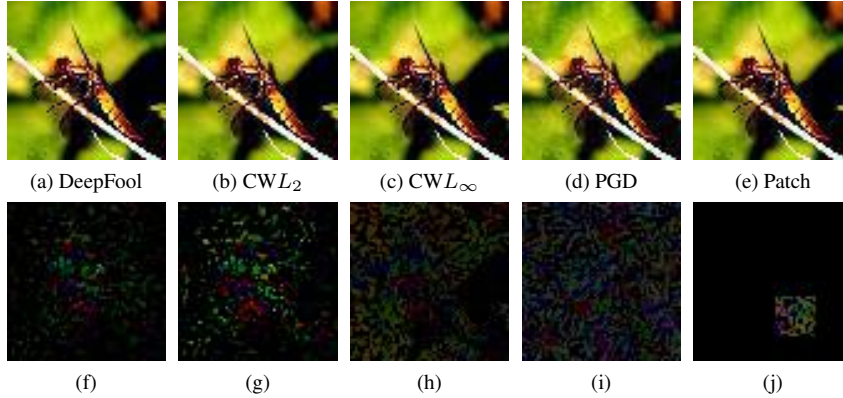


Figure 2. Adversarial Samples (first row) and their respective relatively sparse perturbations (second row), generated based on a ResNext50 network trained on the Tiny ImageNet dataset [41]. Note for the purpose of visualization, second row images have been multiplied by a factor to become visible.

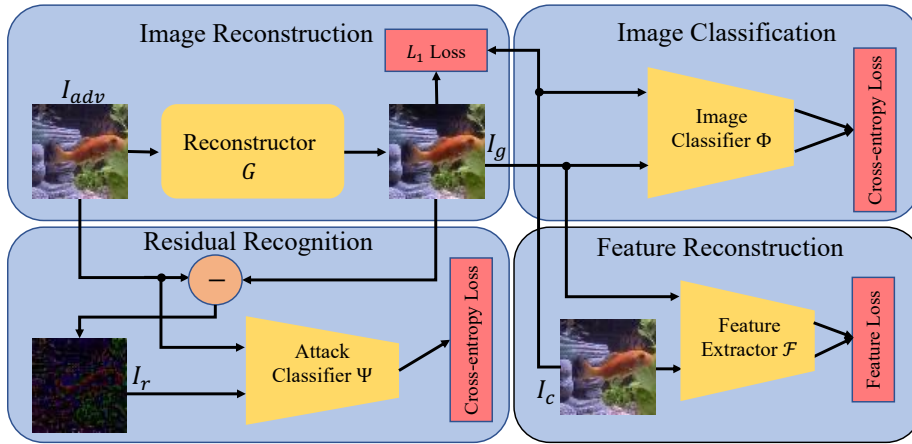


Figure 3. Adversarial Perturbation Recovery via Reverse Engineering of Deceptions via Residual Learning (REDRL) Pipeline. Network G reconstructs the input adversarial image I_{adv} and generates I_g to lie close to the corresponding clean image I_c in L_1 distance. I_g should also result in a high classification score passing through the frozen image classifier Φ trained on I_c . Additionally, G produces I_g so that its extracted features by general feature extractor \mathcal{F} , lie close to that of I_c . To recognize an attack type, generated image I_g is subtracted from the input I_{adv} to obtain the residual image I_r , an estimate of adversarial perturbation. Subsequently, Ψ model classifies concatenation of I_r with its respective I_{adv} into its corresponding class.

4.3. Image Classification

Moreover, REDRL ensures that its reconstructions do not affect the output of an image classifier Φ , trained on clean images. If G is successful at salvaging the critical components of I_c and modeling its distribution, Φ should yield similar classification scores on I_g and I_c . This objective can be framed in the context of Knowledge Distillation [3]. To this end, we introduce the following cross-entropy loss function to REDRL when training G :

$$\mathcal{L}_{IC}(G) = \mathbb{E}_{I_c, \delta} \left[-\log \left(\frac{e^{\Phi_i(G(I_c + \delta))}}{\sum_{j=1}^C e^{\Phi_j(G(I_c + \delta))}} \right) \right] \quad (3)$$

In Eq. 3, i , Φ_i , and C are the argmax $\Phi(I_c)$, i^{th} logit in the output of Φ , and the total number of image classes, respec-

tively. During the training of REDRL, the parameters of Φ are frozen and the gradients from \mathcal{L}_{IC} are back-propagated through the reconstructor G to ensure that I_g is similar to I_c in the view of an image classifier.

4.4. Residual Recognition

Finally, the residual recognition objective subtracts the generated image from the input to obtain the residual image I_r . As REDRL seeks to generate an image close to the clean images manifold, I_r is a reasonable estimate of adversarial perturbations. Next, I_r is fed to the attack classification network Ψ to be classified into one of the respective adversarial attack algorithm classes.

The end goal of REDRL is to estimate the adversarial perturbations and recognize their parent algorithms. There-

Table 1. Image classification accuracy (%) of different image classification models Φ over test set of **clean** samples for CIFAR-10 and Tiny ImageNet datasets.

| Dataset | Model Architecture | | | |
|---------------|--------------------|-----------|-------------|-------|
| | ResNet50 | ResNext50 | DenseNet121 | VGG19 |
| CIFAR-10 | 94.02 | 94.76 | 94.48 | 95.73 |
| Tiny ImageNet | 65.18 | 68.05 | 65.03 | 64.89 |

fore, as the network G reconstructs the input I_{adv} to be close to its corresponding clean image I_c , I_g is subtracted from I_{adv} to obtain the residual image, I_r , an estimate of the adversarial perturbation. Consequently, much of the remaining information in the residual image is representative of the signature of the attack that can be used in its recognition. The attack recognition model Ψ is trained to classify the concatenation of I_{adv} and I_r into the desired class through the attack classification cross-entropy loss function

$$\mathcal{L}_{AC}(G) = \mathbb{E}_{I_c, \delta} \left[-\log \left(\frac{e^{\Psi_i(I_r, I_c + \delta)}}{\sum_{j=1}^A e^{\Psi_j(I_r, I_c + \delta)}} \right) \right] \quad (4)$$

where A , i , and Ψ_j are the total number of considered attack types plus one (for clean data), the true class label corresponding to I_r , and j^{th} logit of $\Psi(I_r, I_{adv})$, respectively. It is noteworthy to mention that the gradient generated from \mathcal{L}_{AC} also back-propagates through the network G so that the obtained residuals carry information needed for attack recognition.

4.5. End-To-End Training

The four stages of REDRL are trained simultaneously in an end-to-end fashion for the purpose of adversarial perturbations estimation and attack algorithm recognition. Altogether, the optimization objective for the end-to-end training of REDRL can be calculated as follows:

$$\mathcal{L}_{total} = \min_G \left[\mathcal{L}_{AC}(G) + \lambda_1 \mathcal{L}_R(G) + \lambda_2 \mathcal{L}_F(G) + \lambda_3 \mathcal{L}_{IC}(G) \right] \quad (5)$$

In Eq. 5, weights λ_1 , λ_2 , and λ_3 are empirically set to 0.01, 0.1, and 1.0, respectively.

4.6. Implementation Details

In this section, we discuss the implementation details of the proposed REDRL and its different modules.

For both CIFAR-10 and Tiny ImageNet, ResNet50, ResNext50, DenseNet121 and VGG19 are used for the choices of architecture of Φ . Table 1 reports the accuracy of different Φ models on the clean test data after being optimized for 50 epochs with Stochastic Gradient Descent with Nesterov Momentum [36], initial learning rate of 0.01 and learning rate decay factor of 10 on 25th and 40th epochs. Using the trained image classifiers, and the five attack algorithms discussed in subsection 3.2, we create attacked

versions of CIFAR-10 and Tiny ImageNet datasets. Table 2 summarizes the configurations and hyper-parameters we used for each attack to create the respective adversarial datasets.

Table 2. Adversarial Attacks Settings

| Attack Type | Configuration |
|-------------------|---|
| DeepFool | Steps: 50 |
| PGD | $\epsilon \in \{4, 8, 16\}$ |
| | $\alpha : 0.01$, Steps: 100 |
| CWL_2 | Steps: 1000, $c \in \{100, 1000\}$ |
| | Learning Rate: 0.01, $\kappa : 0$ |
| CWL_∞ | Steps: 100, $\epsilon \in \{4, 8, 16\}$ |
| | Learning Rate: 0.005, $c : 5$ |
| Adversarial Patch | Steps: 100, $\epsilon \in \{4, 8, 16\}$ |
| | Patch Size $\in \{4 \times 4, 8 \times 8, 16 \times 16\}$ |

As mentioned in subsection 4.1, for the reconstructor network G , we use a cascade of residual blocks without batch normalization layer and skip connections. Moreover, for the residual recognition network Ψ , we consider ResNet18 model to recognize different attack types based on the concatenation of computed residual I_r with the respective adversarial image I_{adv} . To prevent Ψ from overfitting the training data and latching onto undesired patterns in the residuals, we use the label smoothing technique proposed in [37]. Lastly, the REDRL pipeline is trained end-to-end, with a learning rate warm-up technique [6] in the first 10 epochs that has been shown to contribute to the improved recognition performance of DCNNs. In total REDRL is trained for 100 epochs with the Adam optimizer [16] and learning rates of 0.00035 and 0.00017 for CIFAR-10 and Tiny ImageNet datasets, respectively.

4.7. Experimental Evaluation

In section 1, we performed two experiments to show whether it is possible to distinguish adversarial attack types based on their signatures. In addition, Figure 1 demonstrates the degree to which this distinguishability varies from adversarial images I_{adv} to adversarial perturbations δ . Consequently, in the absence of true perturbations and with the goal of having high attack recognition capability, we propose REDRL to estimate adversarial perturbations, *i.e.* I_r . Here we present the evaluation results of REDRL and highlight how the recognition performance gap from adversarial images and adversarial perturbations as seen in Figure 1, can be compensated with the help of residual images.

From Table 3 we can see compared to using only adversarial images I_{adv} , there is a significant boost in the accuracy of the adversarial attack recognition when the concatenation of residual and adversarial images is used. For CIFAR-10 and Tiny ImageNet datasets, the performance improvement of REDRL over attack recognition based on

Table 3. Performance comparison (%) of attack algorithm type recognition based on adversarial images I_{adv} , concatenation of ground-truth adversarial perturbations δ with I_{adv} , and concatenation of estimated residuals I_r with I_{adv} , *i.e.*, REDRL.

| Class | Dataset | | | | | |
|--------------|-----------------|-------------------|----------------|-----------------|-------------------|----------------|
| | CIFAR-10 | | | Tiny ImageNet | | |
| | Input to Ψ | | | Input to Ψ | | |
| | I_{adv} | δ, I_{adv} | I_r, I_{adv} | I_{adv} | δ, I_{adv} | I_r, I_{adv} |
| Clean | 12.0 | 100 | 100 | 62.5 | 99.9 | 99.7 |
| PGD | 73.5 | 99.9 | 99.9 | 88.7 | 99.7 | 99.9 |
| DeepFool | 56.2 | 99.9 | 97.4 | 53.2 | 64.0 | 75.3 |
| CWL_2 | 73.4 | 98.6 | 96.6 | 28.0 | 96.4 | 66.3 |
| CWL_∞ | 33.4 | 71.6 | 74.1 | 24.2 | 92.7 | 57.7 |
| Patch | 58.4 | 99.9 | 99.9 | 73.8 | 99.9 | 99.6 |
| Total | 57.5 | 94.2 | 94.2 | 59.4 | 95.7 | 85.5 |

merely adversarial images is 63% and 43% respectively, showing the power of employing residuals in the estimation of sparse perturbations. Note that numbers under the (δ, I_{adv}) columns show the accuracy if we had access to the ground-truth perturbations. Further, we note that the overall performance on CIFAR-10 is higher. CIFAR-10 has a much lower number of image classes and diversity. In contrast, the Tiny ImageNet has a variety of object classes and high diversity, making it more challenging for the reconstructor network G to correctly model the distribution of the clean images. Another point to observe is that in the case of the Tiny ImageNet dataset, correctly classifying DeepFool, CWL_2 , and CWL_∞ attacks is more challenging for the network Ψ compared to the rest of the classes. This can be attributed to the fact the victim image classifiers performance is relatively inferior compared to the ones for the CIFAR-10 dataset as reported in Table 1. Therefore, the gradient signal back-propagating from \mathcal{L}_{IC} loss, is not as informative as in the case of the CIFAR-10 dataset. Figure 4 shows sample attacked images and the corresponding reconstructed and sparse residual images produced by REDRL. In addition, we would like to understand how well the reconstructor network G in the REDRL pipeline can recover the original image contents from the input adversarial images. To this end, we report the performance of ResNet50, ResNext50, DenseNet121, and VGG19 image classification models on the test set samples and their respective reconstructed counterparts in Table 4. Note that the test sets have both clean and adversarial samples. Table 4 shows the impact of the trained reconstructor G by comparing classification accuracy of images before and after being applied to the reconstructor G . It can be observed that not only image classification accuracy significantly increases for reconstructed attacked images of different types, the accuracy on reconstructed clean samples is maintained. This is consistent across different datasets and different image classification architectures.

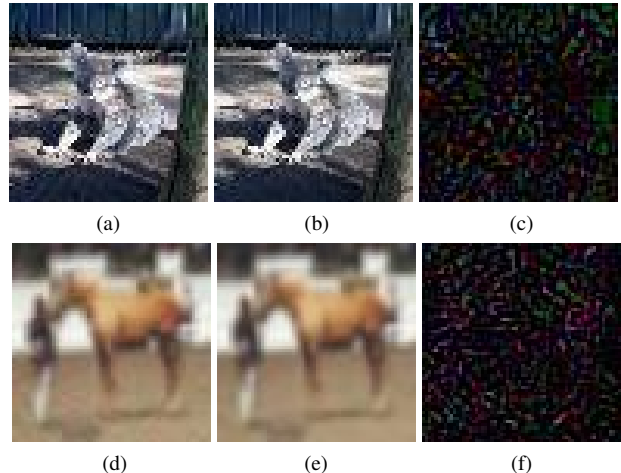


Figure 4. Sample adversarial, reconstructed and residual images in first, second and third columns respectively. First row is sampled from Tiny ImageNet and the second one is from CIFAR-10 dataset. Attack types from top to down are PGD and CWL_2 . Note that pixel values of residual images are multiplied by a factor of 8 for the purpose of visualization.

4.8. Ablation Studies

In this section, we evaluate our design choices for the proposed REDRL to better understand the contribution of Feature Reconstruction (FR) and Image Classification (IC) stages to the residual learning task. Therefore we compare the following three scenarios:

- A. Here we ignore FR and IC stages and only optimize network G for $\mathcal{L}_R(G)$ and $\mathcal{L}_{AC}(G)$.
- B. In this scenario, \mathcal{L}_F is added so that network G is optimized for $\mathcal{L}_R(G)$, $\mathcal{L}_F(G)$, and $\mathcal{L}_{AC}(G)$ objectives.
- C. We investigate the effect of image classification on the overall performance. Therefore, G is trained for $\mathcal{L}_R(G)$, $\mathcal{L}_{IC}(G)$, and \mathcal{L}_{AC} optimization functions.

Table 5 presents how each step of the proposed REDRL can impact the downstream task of attack recognition. Note that in both CIFAR-10 and Tiny ImageNet datasets, REDRL consistently outperforms the rest of the scenarios in terms of overall attack detection accuracy. This shows that enforcing FR and IC constraints simultaneously helps to learn more representative residual. It is noteworthy to mention that we observe Image Classification module in REDRL significantly contributes to the high classification score on reconstructed images.

5. Saliency Profiles

In the previous section, we observed that adversarial attack algorithms generate distinct and identifiable patterns.

Table 4. Comparison of image classification accuracy (%) of different classification models on images before and after being applied to the reconstructor network G . Note that I and $G(I)$ represent input images to and reconstructed images from G respectively.

| Network | CIFAR-10 | | | | | | | | | | | |
|-------------|----------|--------|----------|--------|------|--------|---------|--------|--------------|--------|-------|--------|
| | Clean | | DeepFool | | PGD | | CWL_2 | | CWL_∞ | | Patch | |
| | I | $G(I)$ | I | $G(I)$ | I | $G(I)$ | I | $G(I)$ | I | $G(I)$ | I | $G(I)$ |
| ResNet50 | 94.0 | 94.0 | 7.4 | 87.6 | 2.1 | 90.9 | 0.1 | 88.2 | 13.5 | 85.0 | 79.0 | 93.3 |
| ResNext50 | 94.7 | 94.7 | 8.0 | 87.0 | 2.41 | 91.3 | 0.0 | 85.5 | 12.2 | 85.3 | 80.3 | 94.0 |
| DenseNet121 | 94.4 | 94.4 | 7.9 | 86.3 | 2.1 | 90.6 | 0.6 | 80.9 | 13.0 | 84.1 | 78.6 | 93.7 |
| VGG19 | 95.7 | 95.7 | 8.4 | 87.1 | 2.0 | 93.1 | 0.2 | 84.3 | 5.4 | 86.2 | 75.8 | 94.9 |

| Network | Tiny ImageNet | | | | | | | | | | | |
|-------------|---------------|--------|----------|--------|-----|--------|---------|--------|--------------|--------|-------|--------|
| | Clean | | DeepFool | | PGD | | CWL_2 | | CWL_∞ | | Patch | |
| | I | $G(I)$ | I | $G(I)$ | I | $G(I)$ | I | $G(I)$ | I | $G(I)$ | I | $G(I)$ |
| ResNet50 | 65.1 | 65.1 | 11.5 | 51.3 | 0.3 | 37.8 | 0.1 | 39.5 | 2.7 | 40.9 | 48.5 | 61.0 |
| ResNext50 | 68.0 | 68.0 | 11.2 | 53.9 | 0.4 | 36.6 | 0.1 | 36.5 | 3.1 | 43.5 | 51.6 | 63.8 |
| DenseNet121 | 65.0 | 64.9 | 11.8 | 53.2 | 0.1 | 27.3 | 0.1 | 31.6 | 3.2 | 39.0 | 48.8 | 60.4 |
| VGG19 | 64.8 | 64.8 | 11.1 | 45.9 | 0.2 | 26.1 | 0.0 | 31.5 | 1.6 | 34.1 | 45.7 | 59.5 |

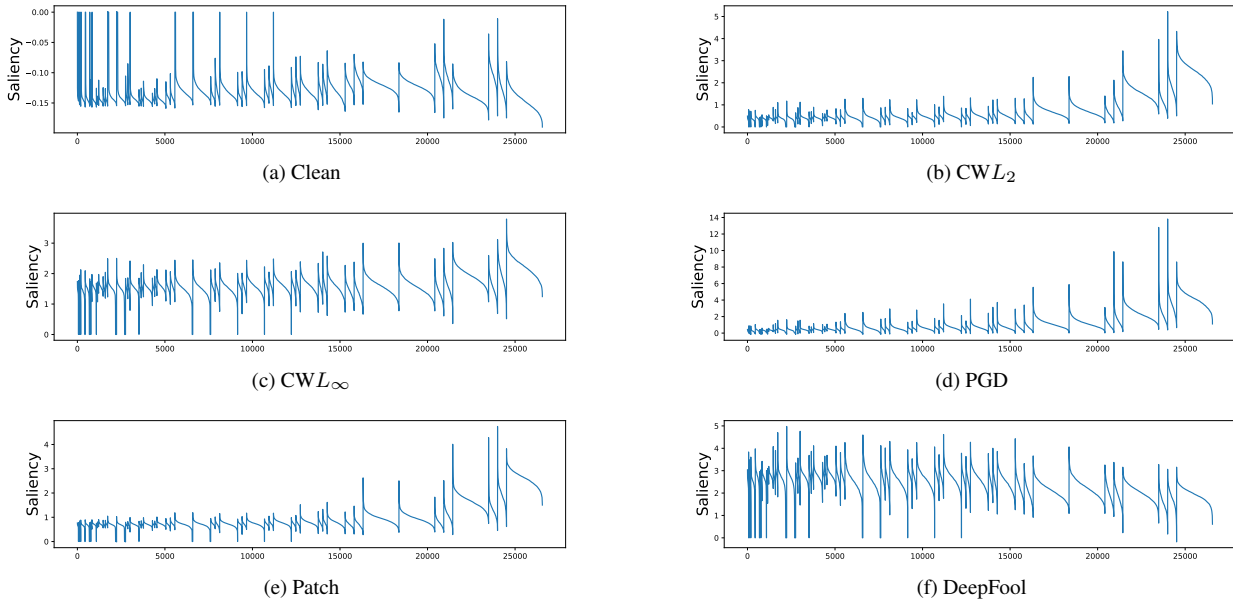


Figure 5. Parameter saliency profiles for different adversarial attacks on CIFAR-10 and using ResNet50 image classifier. Perturbations used for PGD and CWL_∞ have L_∞ -norm bounded by $16/255$. Note the magnitude of saliency profiles on y-axis when comparing different attacks. Details of different attacks are presented in supplementary material.

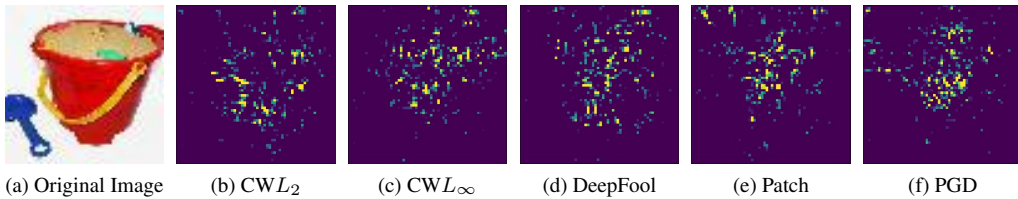


Figure 6. Input saliency heat-maps for different adversarial attacks on Tiny ImageNet using ResNet50 image classifier. Perturbations used for PGD and CWL_∞ have L_∞ -norm bounded by $16/255$. We can observe from the figures that each attack has a specific saliency heat-map. Details of different attacks are presented in supplementary material.

Table 5. Investigating the effects of Feature Reconstruction (\mathcal{L}_F) and Image Classification (\mathcal{L}_{IC}) objectives on the adversarial attack recognition accuracy (%).

| Class | Dataset | | | | | | | |
|--------------|----------|-------|-------|--------------|---------------|------|-------|--------------|
| | CIFAR-10 | | | | Tiny ImageNet | | | |
| | A | B | C | REDRL | A | B | C | REDRL |
| Clean | 99.9 | 98.9 | 100 | 100 | 99.8 | 99.5 | 99.5 | 99.7 |
| DeepFool | 99.3 | 98.8 | 99.8 | 97.4 | 87.1 | 93.8 | 71.9 | 75.3 |
| PGD | 99.9 | 99.6 | 99.9 | 99.9 | 99.9 | 99.8 | 99.9 | 99.9 |
| CWL_2 | 84.2 | 88.7 | 93.3 | 96.6 | 58.7 | 60.2 | 61.5 | 66.3 |
| CWL_∞ | 63.3 | 70.8 | 71.6 | 74.1 | 42.9 | 43.0 | 53.8 | 57.7 |
| Patch | 99.7 | 99.8 | 99.9 | 99.9 | 98.6 | 98.9 | 99.2 | 99.6 |
| Total | 90.59 | 92.58 | 93.51 | 94.28 | 81.9 | 82.7 | 83.72 | 85.57 |

This observation raises the question, do different attacks yield qualitatively different downstream behavior in neural networks? To answer this question, we make use of recent work in parameter-space saliency maps [20].

5.1. Parameter-Space Saliency Maps

One intuitive approach to parameter space saliency would involve simply obtaining the gradient of the loss with respect to the parameters on a sample of interest and computing its entry-wise absolute value. The authors of [20] note that early layers typically exhibit higher saliency under this definition since their filters extract broadly applicable low-level features and errors propagated from early layers accumulate during a forward pass, yet this phenomenon does not imply that early filters are responsible for misbehavior specific to the sample of interest. Thus, they standardize the saliency values across the entire validation set so that saliency for a particular parameter now represents the number of standard deviations away from the mean saliency value (of that parameter) over validation samples. Additionally, the authors note that individual filters are often responsible for interpretable tasks, so they aggregate saliency by filter. Finally, saliency can be written as

$$\hat{s}_k(x, y) := \frac{\frac{1}{|\alpha_k|} \sum_{i \in \alpha_k} |\nabla_{\theta_i} \mathcal{L}_\theta(x, y)| - \mu_k}{\sigma_k}, \quad (6)$$

where μ_k and σ_k denote the mean and standard deviation, respectively, of $\frac{1}{|\alpha_k|} \sum_{i \in \alpha_k} |\nabla_{\theta_i} \mathcal{L}_\theta(x, y)|$ across all (x, y) pairs in the validation set, and α_k denotes all indices of parameters belonging to filter k . We use this definition of saliency in our subsequent experiments. By plotting such saliency maps, we can identify exactly where in the network an adversarial attack triggers malicious behavior.

The authors of [20] further use this method to compute input-space saliency maps, $M_F = |\nabla_x D_C(\hat{s}(x, y), \hat{s}')|$, where D_C denotes cosine distance, and \hat{s}' is a copy of $\hat{s}(x, y)$ in which entries corresponding to the top n most salient filters are boosted. We will also use these input-space saliency maps to analyze the distinct patterns of adversarial attacks. These input-space maps indicate exactly

which input features are triggering the misbehaviors identified in parameter space.

Figure 5 contains the saliency profiles of clean images and adversarial examples on the CIFAR-10 dataset using a ResNet50 model, where filters in each layer are sorted from most to least salient as in [20] and then the profiles are averaged over the entire test set. We observe that each attack has a unique and dramatically different saliency map. For example, we see that PGD, CWL_2 , and the Patch attack mostly target the final layers, while DeepFool focuses on the earlier layers, and CWL_∞ targets almost all layers. These observations are consistent across different datasets and architectures (see supplementary materials for additional saliency profiles). Note that even though PGD, CWL_2 , and Adversarial Patch seem to yield similar saliency profiles, they have different magnitudes, *i.e.* different values on the y-axis.

Figure 6 depicts the previously described input-space visualizations derived from the parameter-space saliency maps. We see that different attacks highlight distinct image-space regions. This observation indicates that the model’s filters which are triggered most by an attack, perform different functions across the various attacks we examine. We conclude from these heat-maps that different attacks have qualitatively different impacts on the behavior of the victims models.

6. Conclusion

Adversarial attack algorithms are historically compared only by their success rates at fooling victim models. We find that these attacks produce distinct perturbation patterns which can be classified from the adversarial example alone (without access to the perturbation itself). In order to do so, we present a novel end-to-end framework, REDRL, for extracting adversarial perturbations from perturbed images and classifying the parent adversary. Moreover, we use parameter-space saliency profiles to investigate the downstream effects of adversarial attacks on their victims and find unique attack-specific behavior. Namely, some attacks (*e.g.*, PGD) trigger misbehavior in deeper components of the victim architecture, while others (*e.g.*, DeepFool) primarily target shallow components. We conclude from these exploratory experiments that adversarial examples do not simply differ in effectiveness, and our work leaves open the possibility that practitioners deciding on an attack for their use-case should consider qualitative impacts other than simply the success rate at degrading test accuracy.

References

- [1] Tom B Brown, Dandelion Mané, Aurko Roy, Martín Abadi, and Justin Gilmer. Adversarial patch. *arXiv preprint arXiv:1712.09665*, 2017.

- [2] Nicholas Carlini and David Wagner. Towards evaluating the robustness of neural networks. In *2017 IEEE Symposium on Security and Privacy (SP)*, pages 39–57. IEEE, 2017.
- [3] Hanting Chen, Yunhe Wang, Chang Xu, Zhaohui Yang, Chuanjian Liu, Boxin Shi, Chunjing Xu, Chao Xu, and Qi Tian. Data-free learning of student networks. In *Proceedings of the IEEE/CVF International Conference on Computer Vision (ICCV)*, October 2019.
- [4] Valeriia Cherepanova, Micah Goldblum, Harrison Foley, Shiyuan Duan, John Dickerson, Gavin Taylor, and Tom Goldstein. Lowkey: leveraging adversarial attacks to protect social media users from facial recognition. *arXiv preprint arXiv:2101.07922*, 2021.
- [5] Jia Deng, Wei Dong, Richard Socher, Li-Jia Li, Kai Li, and Li Fei-Fei. Imagenet: A large-scale hierarchical image database. In *2009 IEEE conference on computer vision and pattern recognition*, pages 248–255. Ieee, 2009.
- [6] Xing Fan, Wei Jiang, Hao Luo, and Mengjuan Fei. Sphered: Deep hypersphere manifold embedding for person re-identification. *Journal of Visual Communication and Image Representation*, 60:51–58, 2019.
- [7] Reuben Feinman, Ryan R Curtin, Saurabh Shintre, and Andrew B Gardner. Detecting adversarial samples from artifacts. *arXiv preprint arXiv:1703.00410*, 2017.
- [8] Ross Girshick, Jeff Donahue, Trevor Darrell, and Jitendra Malik. Rich feature hierarchies for accurate object detection and semantic segmentation. In *Proceedings of the IEEE conference on computer vision and pattern recognition*, pages 580–587, 2014.
- [9] Micah Goldblum, Liam Fowl, Soheil Feizi, and Tom Goldstein. Adversarially robust distillation. In *Proceedings of the AAAI Conference on Artificial Intelligence*, volume 34, pages 3996–4003, 2020.
- [10] Micah Goldblum, Avi Schwarzschild, Ankit B Patel, and Tom Goldstein. Adversarial attacks on machine learning systems for high-frequency trading. *arXiv preprint arXiv:2002.09565*, 2020.
- [11] Kathrin Grosse, Praveen Manoharan, Nicolas Papernot, Michael Backes, and Patrick McDaniel. On the (statistical) detection of adversarial examples. *arXiv preprint arXiv:1702.06280*, 2017.
- [12] Kaiming He, Xiangyu Zhang, Shaoqing Ren, and Jian Sun. Deep residual learning for image recognition. In *Proceedings of the IEEE conference on computer vision and pattern recognition*, pages 770–778, 2016.
- [13] P. Isola, J. Zhu, T. Zhou, and A. A. Efros. Image-to-image translation with conditional adversarial networks. In *2017 IEEE Conference on Computer Vision and Pattern Recognition (CVPR)*, pages 5967–5976, 2017.
- [14] Danny Karmon, Daniel Zoran, and Yoav Goldberg. Lavan: Localized and visible adversarial noise. *arXiv preprint arXiv:1801.02608*, 2018.
- [15] Pirazh Khorramshahi, Neehar Peri, Jun cheng Chen, and Rama Chellappa. The devil is in the details: Self-supervised attention for vehicle re-identification, 2020.
- [16] Diederik P Kingma and Jimmy Ba. Adam: A method for stochastic optimization. *arXiv preprint arXiv:1412.6980*, 2014.
- [17] Alex Krizhevsky, Geoffrey Hinton, et al. Learning multiple layers of features from tiny images. 2009.
- [18] Alex Krizhevsky, Ilya Sutskever, and Geoffrey E Hinton. Imagenet classification with deep convolutional neural networks. *Communications of the ACM*, 60(6):84–90, 2017.
- [19] Christian Ledig, Lucas Theis, Ferenc Huszár, Jose Caballero, Andrew Cunningham, Alejandro Acosta, Andrew Aitken, Alykhan Tejani, Johannes Totz, Zehan Wang, et al. Photo-realistic single image super-resolution using a generative adversarial network. In *Proceedings of the IEEE conference on computer vision and pattern recognition*, pages 4681–4690, 2017.
- [20] Roman Levin, Manli Shu, Eitan Borgnia, Furong Huang, Micah Goldblum, and Tom Goldstein. Where do models go wrong? parameter-space saliency maps for explainability. *arXiv preprint arXiv:2108.01335*, 2021.
- [21] Wei-An Lin, Chun Pong Lau, Alexander Levine, Rama Chellappa, and Soheil Feizi. Dual manifold adversarial robustness: Defense against lp and non-lp adversarial attacks, 2020.
- [22] Wei Liu, Dragomir Anguelov, Dumitru Erhan, Christian Szegedy, Scott Reed, Cheng-Yang Fu, and Alexander C Berg. Ssd: Single shot multibox detector. In *European conference on computer vision*, pages 21–37. Springer, 2016.
- [23] Aleksander Madry, Aleksandar Makelov, Ludwig Schmidt, Dimitris Tsipras, and Adrian Vladu. Towards deep learning models resistant to adversarial attacks. *arXiv preprint arXiv:1706.06083*, 2017.
- [24] Jan Hendrik Metzen, Tim Genewein, Volker Fischer, and Bastian Bischoff. On detecting adversarial perturbations. *arXiv preprint arXiv:1702.04267*, 2017.
- [25] Seyed-Mohsen Moosavi-Dezfooli, Alhussein Fawzi, and Pascal Frossard. Deepfool: a simple and accurate method to fool deep neural networks. In *Proceedings of the IEEE conference on computer vision and pattern recognition*, pages 2574–2582, 2016.
- [26] Muzammal Naseer, Salman Khan, Munawar Hayat, Fahad Shahbaz Khan, and Fatih Porikli. A self-supervised approach for adversarial robustness. In *IEEE/CVF Conference on Computer Vision and Pattern Recognition (CVPR)*, June 2020.
- [27] Alejandro Newell, Kaiyu Yang, and Jia Deng. Stacked hourglass networks for human pose estimation. In *European conference on computer vision*, pages 483–499. Springer, 2016.
- [28] Utku Ozbulak, Baptist Vandersmissen, Azarakhsh Jalalvand, Ivo Couckuyt, Arnout Van Messem, and Wesley De Neve. Investigating the significance of adversarial attacks and their relation to interpretability for radar-based human activity recognition systems. *Computer Vision and Image Understanding*, 202:103111, 2021.
- [29] Nicolas Papernot, Patrick McDaniel, Xi Wu, Somesh Jha, and Ananthram Swami. Distillation as a defense to adversarial perturbations against deep neural networks. In *2016 IEEE Symposium on Security and Privacy (SP)*, pages 582–597. IEEE, 2016.
- [30] Rajeev Ranjan, Vishal M Patel, and Rama Chellappa. Hyperface: A deep multi-task learning framework for face detection, landmark localization, pose estimation, and gender

- recognition. *IEEE Transactions on Pattern Analysis and Machine Intelligence*, 41(1):121–135, 2017.
- [31] Joseph Redmon, Santosh Divvala, Ross Girshick, and Ali Farhadi. You only look once: Unified, real-time object detection. In *Proceedings of the IEEE conference on computer vision and pattern recognition*, pages 779–788, 2016.
- [32] Ramprasaath R Selvaraju, Michael Cogswell, Abhishek Das, Ramakrishna Vedantam, Devi Parikh, and Dhruv Batra. Grad-cam: Visual explanations from deep networks via gradient-based localization. In *Proceedings of the IEEE international conference on computer vision*, pages 618–626, 2017.
- [33] Karen Simonyan, Andrea Vedaldi, and Andrew Zisserman. Deep inside convolutional networks: Visualising image classification models and saliency maps. *arXiv preprint arXiv:1312.6034*, 2013.
- [34] Karen Simonyan and Andrew Zisserman. Two-stream convolutional networks for action recognition in videos. In *Advances in neural information processing systems*, pages 568–576, 2014.
- [35] Karen Simonyan and Andrew Zisserman. Very deep convolutional networks for large-scale image recognition. *arXiv preprint arXiv:1409.1556*, 2014.
- [36] Ilya Sutskever, James Martens, George Dahl, and Geoffrey Hinton. On the importance of initialization and momentum in deep learning. In *International conference on machine learning*, pages 1139–1147. PMLR, 2013.
- [37] Christian Szegedy, Vincent Vanhoucke, Sergey Ioffe, Jon Shlens, and Zbigniew Wojna. Rethinking the inception architecture for computer vision. In *Proceedings of the IEEE conference on computer vision and pattern recognition*, pages 2818–2826, 2016.
- [38] Christian Szegedy, Wojciech Zaremba, Ilya Sutskever, Joan Bruna, Dumitru Erhan, Ian Goodfellow, and Rob Fergus. Intriguing properties of neural networks. *arXiv preprint arXiv:1312.6199*, 2013.
- [39] Oriol Vinyals, Alexander Toshev, Samy Bengio, and Dumitru Erhan. Show and tell: A neural image caption generator. In *Proceedings of the IEEE conference on computer vision and pattern recognition*, pages 3156–3164, 2015.
- [40] Lijun Wang, Wanli Ouyang, Xiaogang Wang, and Huchuan Lu. Visual tracking with fully convolutional networks. In *Proceedings of the IEEE international conference on computer vision*, pages 3119–3127, 2015.
- [41] Jiayu Wu, Qixiang Zhang, and Guoxi Xu. Tiny imagenet challenge. *Technical Report*, 2017.
- [42] Han Xu, Yao Ma, Haochen Liu, Debayan Deb, Hui Liu, Jiliang Tang, and Anil K. Jain. Adversarial attacks and defenses in images, graphs and text: A review, 2019.
- [43] Kaidi Xu, Sijia Liu, Pu Zhao, Pin-Yu Chen, Huan Zhang, Quanfu Fan, Deniz Erdogmus, Yanzhi Wang, and Xue Lin. Structured adversarial attack: Towards general implementation and better interpretability. *arXiv preprint arXiv:1808.01664*, 2018.
- [44] Hongyang Zhang, Yaodong Yu, Jiantao Jiao, Eric Xing, Laurent El Ghaoui, and Michael Jordan. Theoretically principled trade-off between robustness and accuracy. In *International*

Conference on Machine Learning, pages 7472–7482. PMLR, 2019.

Appendix

A. Adversarial Attack Configurations

As mentioned in the paper, we adopted five adversarial attack models, namely, DeepFool, CWL_2 , CWL_∞ , PGD and Adversarial Patch. Therefore, we created five different adversarial versions of CIFAR-10 and Tiny ImageNet datasets for the purpose of our experiments. Table 6 summarizes the configurations and hyper-parameters we used for each attack to create the respective adversarial datasets.

Table 6. Adversarial Attacks Settings

| Attack Type | Configuration |
|-------------------|---|
| DeepFool | Steps: 50 |
| PGD | $\epsilon \in \{4, 8, 16\}$ |
| | $\alpha : 0.01$, Steps: 100 |
| CWL_2 | Steps: 1000, $c \in \{100, 1000\}$ |
| | Learning Rate: 0.01, $\kappa : 0$ |
| CWL_∞ | Steps: 100, $\epsilon \in \{4, 8, 16\}$ |
| | Learning Rate: 0.005, $c : 5$ |
| Adversarial Patch | Steps: 100, $\epsilon \in \{4, 8, 16\}$ |
| | Patch Size $\in \{4 \times 4, 8 \times 8, 16 \times 16\}$ |

In Table 6, Steps represent the number of iterations for which an adversarial perturbation was optimized to maximize the loss an image classification model. In addition, ϵ and α are the maximum allowable perturbation size and the step size in each iteration respectively. For CWL_2 , c is the hyper-parameter which shows the trade-off between the distance and confidence terms in the optimization objective; also κ represents the confidence of adversarial examples.

B. Saliency Profile

B.1. Input-Space Saliency Map

Due to the space constraint, we did not incorporate an example of input-saliency map for CIFAR10 dataset. However, here we show an example of input-space saliency maps for an sample of CIFAR-10 dataset using ResNext50 model.

Similar to Figure 6 in the paper, from Figure 7 we can see that different attack algorithms have different input-saliency maps despite using a fixed image classification model.

B.2. Parameter-space Saliency Profile

In this section we present the averaged parameter-space saliency profile over the test set for CIFAR-10 and Tiny ImageNet dataset and for ResNet50, ResNext50, DenseNet121 and VGG19 image classifiers. Also note that to compute parameter-space saliency profiles, we only use the samples that were originally correctly classified by the image classifier but were miss-classified after being attacked by the attack algorithm.

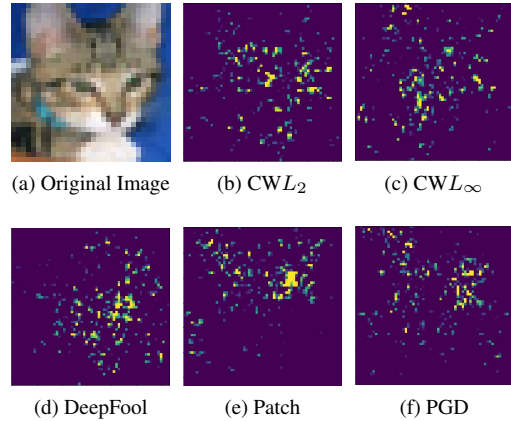


Figure 7. Input saliency heat-maps for different adversarial attacks on CIFAR-10 dataset using ResNet50 image classifier. We can observe from the figures that each attack has a specific saliency heat-map

B.2.1 CIFAR-10

Figures 8, 9, 10 and 11 depict the parameter-saliency profile of different attack algorithms for ResNet50, ResNext50, DenseNet121 and VGG19 image classifiers respectively. Note that the x-axis varies in figures corresponding to different image classification architectures as they have different number of layers and different number of filters for each layer.

Comparing these figures, clearly shows that the effect of adversarial attacks on victim models is specific to attack algorithms and regardless of the victim model’s architecture. In addition, while the saliency profile of CWL_2 , PGD and Patch attacks seems to be similar, their respective saliency profiles are quite different in their magnitude, *i.e.* the y-axis values.

B.2.2 Tiny ImageNet

Figures 12, 13, 14 and 15 show the parameter-saliency profile of different attack types for ResNet50, ResNext50, DenseNet121 and VGG19 image classification networks respectively. Similar to CIFAR-10 dataset, the parameter-saliency profile is attack-specific and irrespective of the target victim model. Additionally, while the examination of parameter-saliency profiles for different models may show differences across CIFAR-10 and Tiny ImageNet datasets, it can be observed that there are qualitative similarities which is consistent for each attack algorithm. The cause for cross dataset differences in saliency profiles can be rooted in the fact that Tiny ImageNet dataset is much more diverse and challenging compared to CIFAR-10.

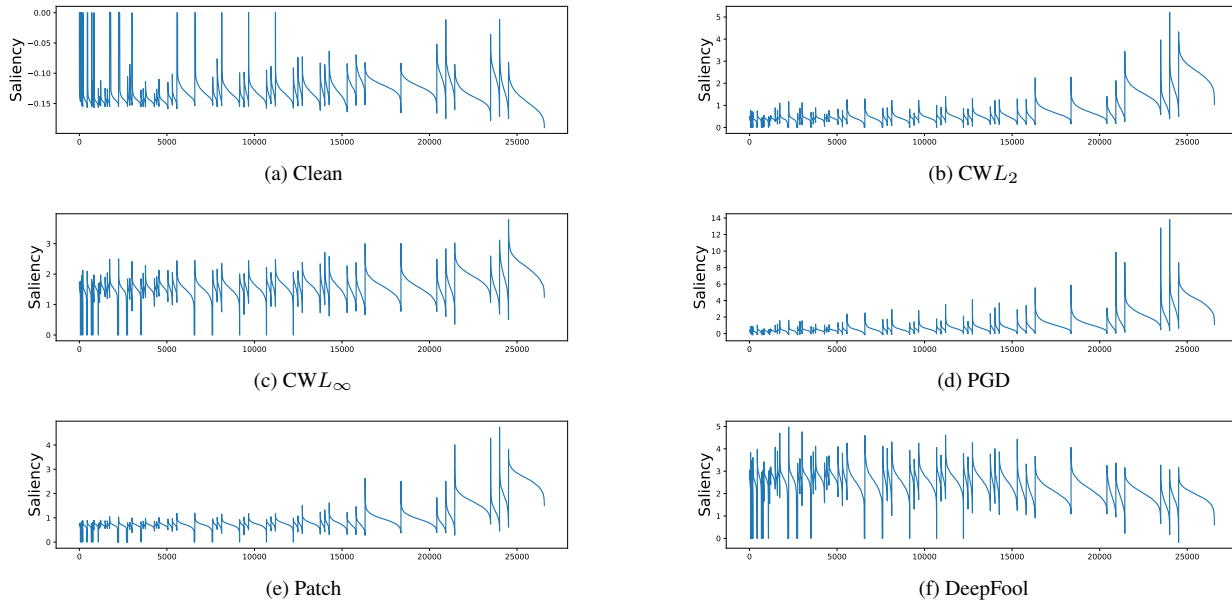


Figure 8. Parameter-space saliency profiles for different adversarial attacks on CIFAR-10 and using ResNet50 image classifier. Note the magnitude of saliency profiles on y-axis when comparing different attacks.

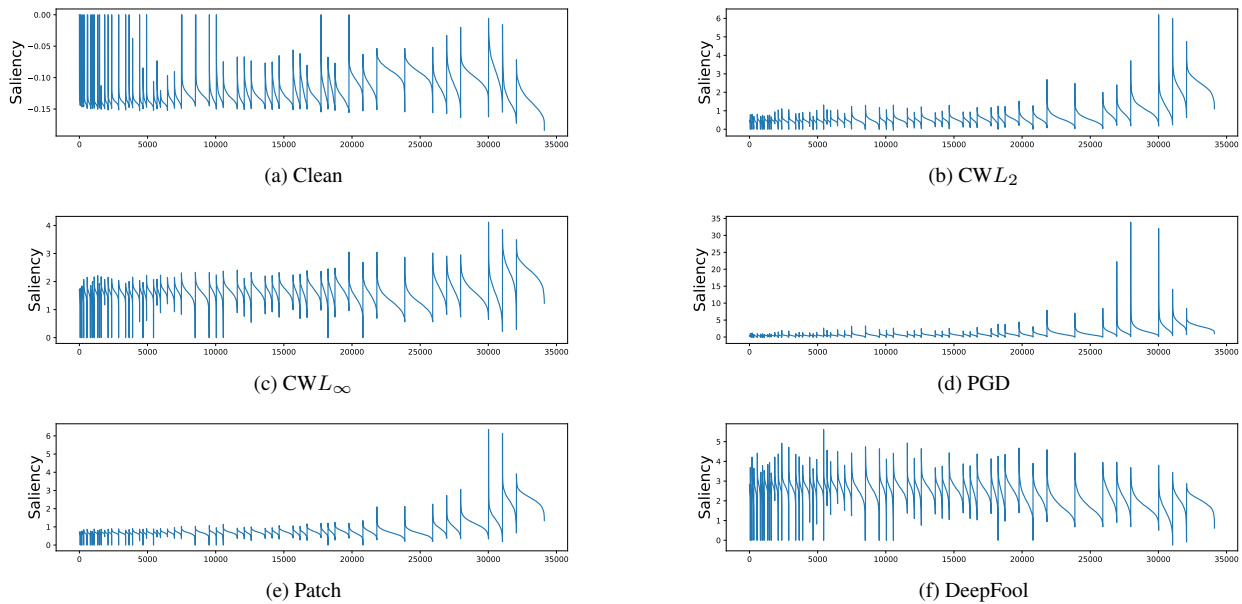


Figure 9. Parameter-space saliency profiles for different adversarial attacks on CIFAR-10 and using ResNext50 image classifier. Note the magnitude of saliency profiles on y-axis when comparing different attacks.

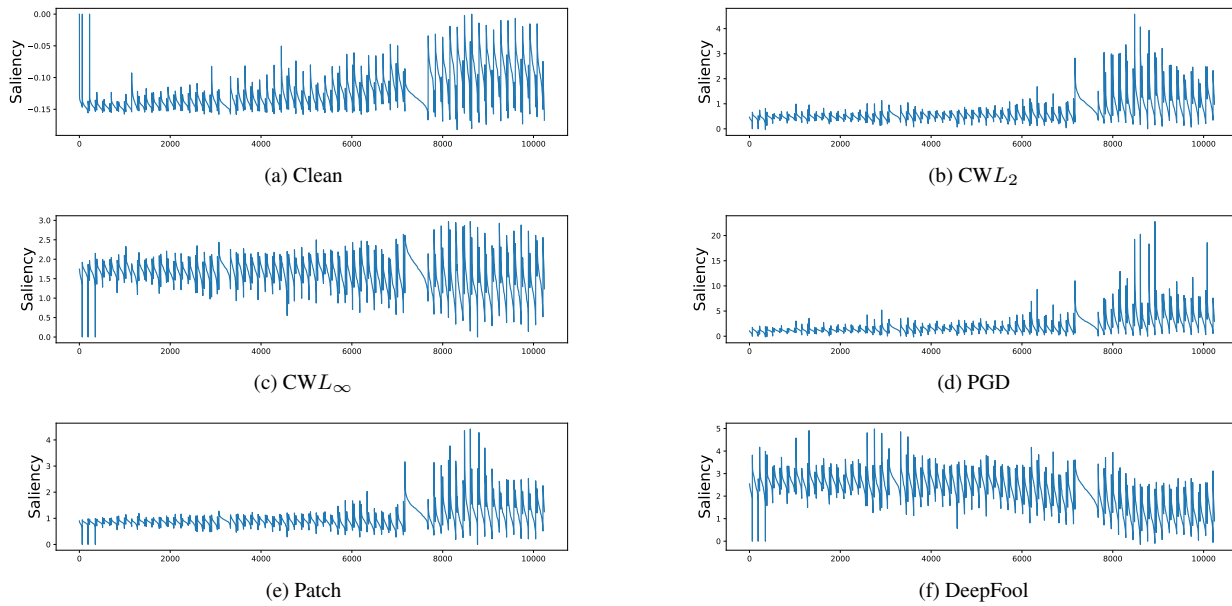


Figure 10. Parameter-space saliency profiles for different adversarial attacks on CIFAR-10 and using DenseNet121 image classifier. Note the magnitude of saliency profiles on y-axis when comparing different attacks.

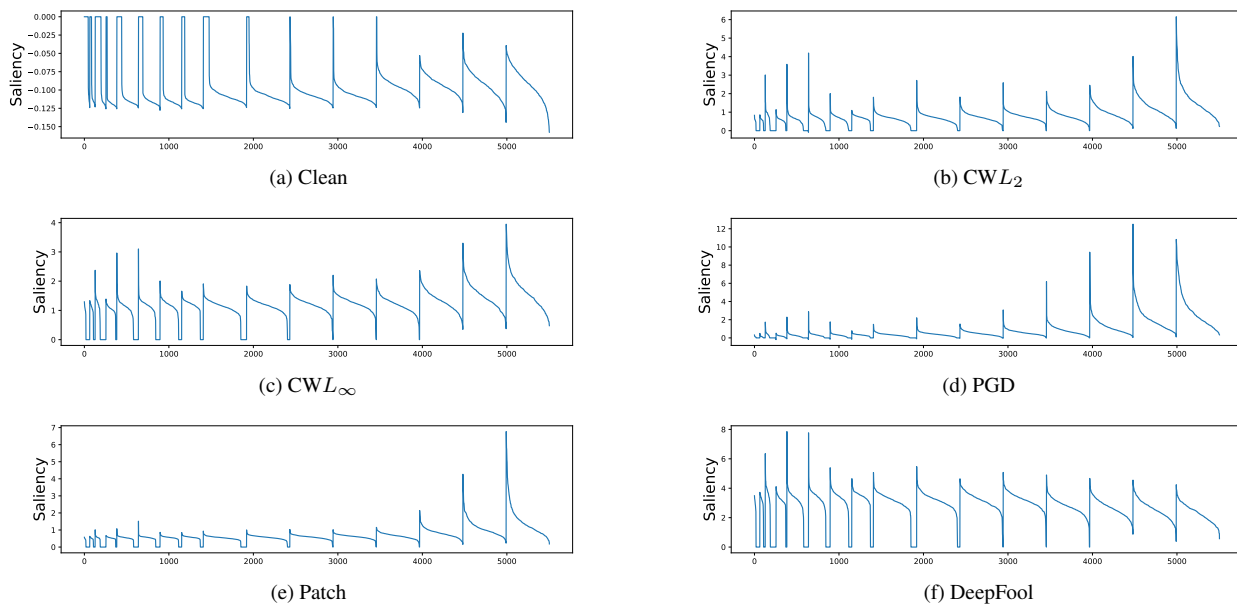


Figure 11. Parameter-space saliency profiles for different adversarial attacks on CIFAR-10 and using VGG19 image classifier. Note the magnitude of saliency profiles on y-axis when comparing different attacks.

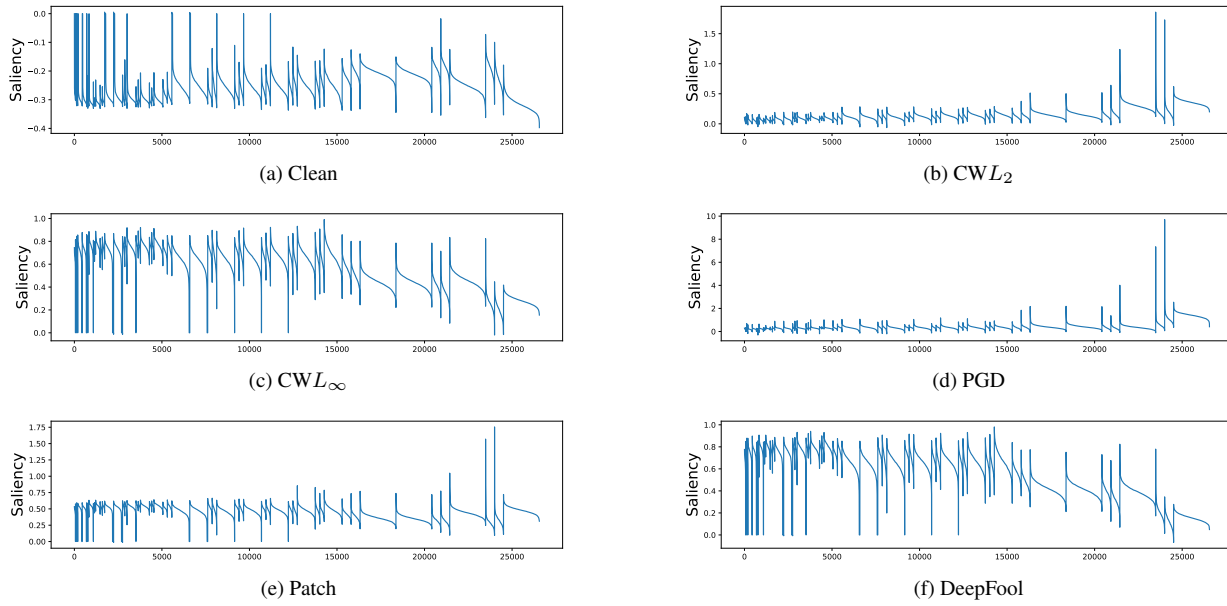


Figure 12. Parameter-space saliency profiles for different adversarial attacks on Tiny ImageNet and using ResNet50 image classifier. Note the magnitude of saliency profiles on y-axis when comparing different attacks.

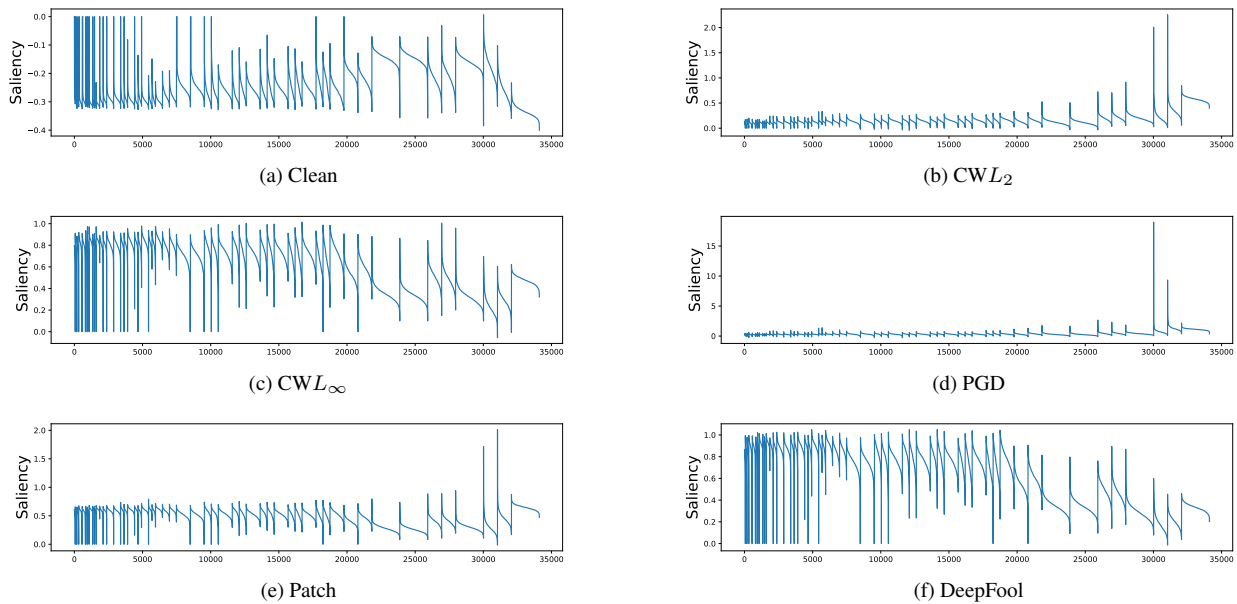


Figure 13. Parameter-space saliency profiles for different adversarial attacks on Tiny ImageNet and using ResNext50 image classifier. Note the magnitude of saliency profiles on y-axis when comparing different attacks.

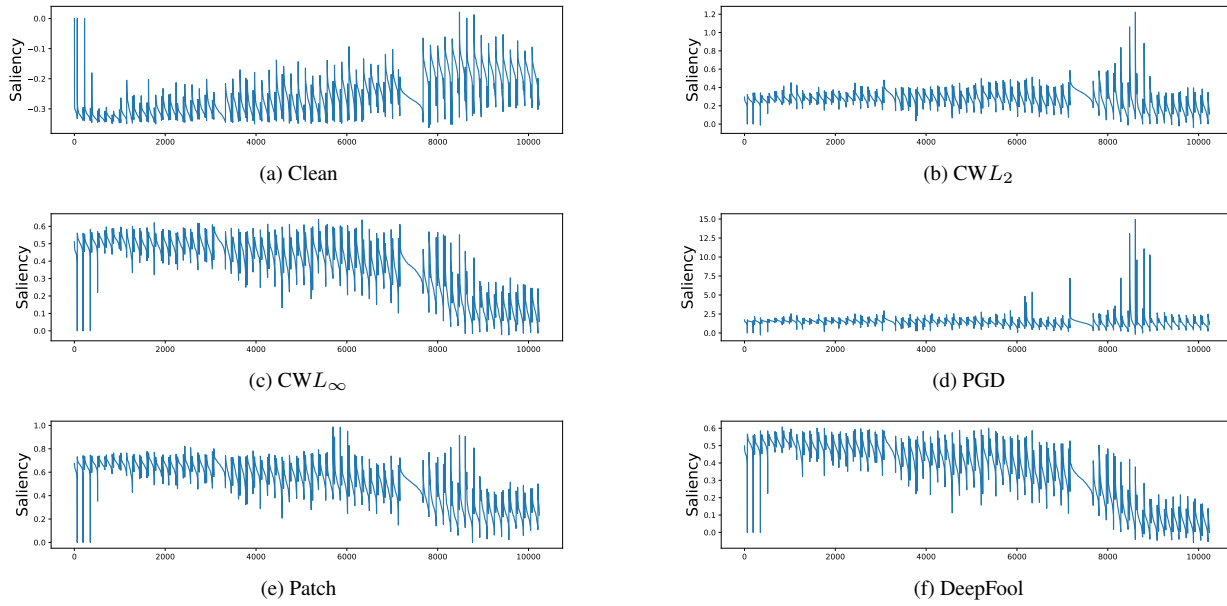


Figure 14. Parameter-space saliency profiles for different adversarial attacks on Tiny ImageNet and using DenseNet121 image classifier. Note the magnitude of saliency profiles on y-axis when comparing different attacks.

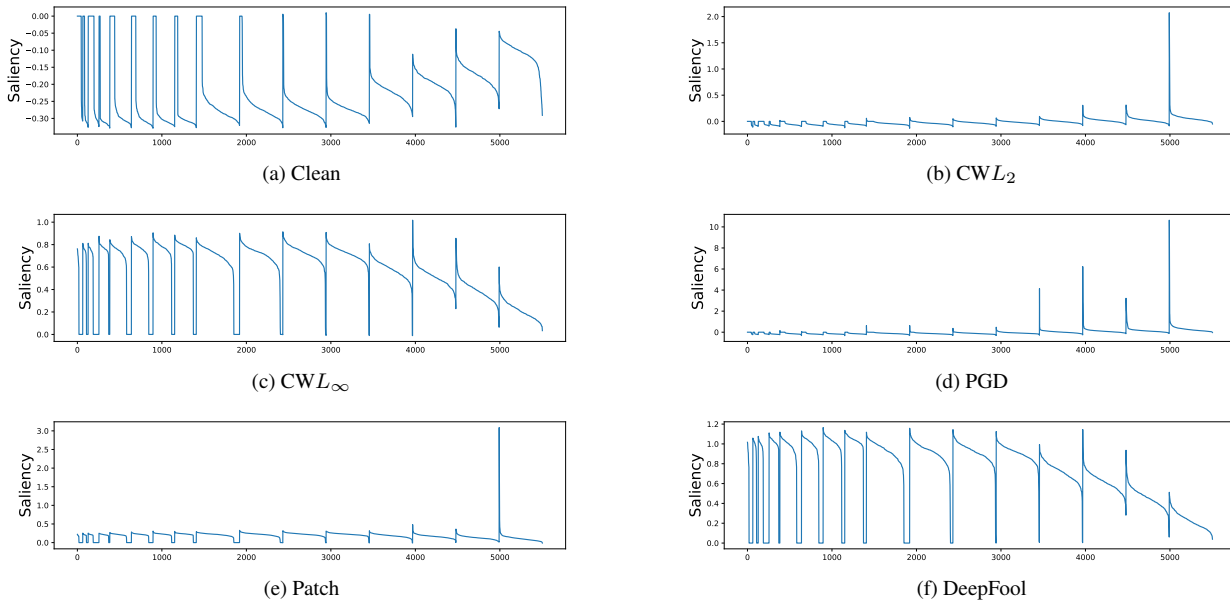


Figure 15. Parameter-space saliency profiles for different adversarial attacks on Tiny ImageNet and using VGG19 image classifier. Note the magnitude of saliency profiles on y-axis when comparing different attacks.